

Relating electrical resistivity to permeability using resistor networks

Alison Kirkby*

University of Adelaide, North Terrace, Adelaide 5005
Geoscience Australia, Symonston, ACT 2609
Alison.Kirkby@adelaide.edu.au

Graham Heinson

University of Adelaide
North Terrace, Adelaide 5005
Graham.Heinson@adelaide.edu.au

Lars Krieger

University of Adelaide
North Terrace, Adelaide 5005
Lars.Krieger@adelaide.edu.au

SUMMARY

We use resistor network models to explore the relationship between electrical resistivity and permeability in fractures filled with an electrically conductive fluid. The fracture aperture distribution is determined by generating fracture surface pairs that are constructed based on characteristics measured on rock samples. We use these to generate and solve resistor networks with variable hydraulic and electrical resistance. The aperture is incrementally increased, to analyse the changes in both properties as a fault is opened. At small apertures, electrical conductivity and permeability increase moderately with aperture until the fault reaches its percolation threshold. Above this point, the permeability increases by four orders of magnitude over a change in mean aperture of less than 0.1 mm, while the resistivity decreases by up to a factor of 10. The permeability increases at a greater rate than the conductivity, and therefore the percolation threshold can be defined in terms of the matrix to fracture resistivity ratio, M . The value of M at the percolation threshold, M_{PT} , varies with the ratio of rock to fluid resistivity, the fault spacing, and the fault offset but is always less than 10. Greater M values are associated with fractures above their percolation threshold and therefore open for fluid flow.

Key words: permeability, resistivity, fractures, faults

INTRODUCTION

Permeability in the crust comprises both primary permeability, from interconnected pore space present at the time of deposition of sedimentary rocks, and secondary permeability, which can result from fractures and faults. Resource industries such as geothermal and oil and gas rely on fracture permeability for reservoir performance, however characterizing the fracture permeability distribution from the surface can be a challenge.

The introduction of an electrically conductive fluid into a fault network has been shown to produce changes in the bulk electrical conductivity that are measurable from the surface using the magnetotelluric (MT) method (Peacock et al. 2012, Peacock et al. 2013, Macfarlane et al. 2014). Magnetotelluric data have also been used to qualitatively infer the permeability of natural fractures (e.g., Kirkby et al. 2015). In these examples, the electrical resistivity was interpreted to vary with orientation, with anisotropy ratios of up to 200 determined from modelling. Characterising the resistivity anisotropy of faults and fractures helps determine the amount by which the faults enhance the conductivity. When the conductivity enhancement can be attributed to fluids contained in the fractures it may be possible to use the resistivity to infer their permeability. This is done in porous rocks by first inferring porosity through models such as Archie's Law (Archie, 1942). However, the amount and distribution of pore space in fractured, low porosity rocks is likely to be different to that in porous rocks, and both fluid flow and electrical conduction rely on the distribution of pore space as well as the total volume (e.g., Brown 1989). Therefore, relating resistivity and permeability directly may be more relevant for deducing the fluid flow properties of fractures and faults.

We present modelling that uses the similarities between the flow of electrical current and fluids to improve our understanding of the relationship between resistivity and permeability in fractured rocks. The work presented here summarises the work of Kirkby et al. (2016). The modelling is carried out on single rough fractures, constructed based on characteristics measured on rock fracture surfaces. Each fracture is progressively opened to investigate the changes in resistivity and permeability as the aperture is increased. This work may help to improve our understanding of resistivity anomalies resulting from the presence of fluid-filled fractures, characterized using techniques such as MT. It may also provide a proxy for experimental measurements of fracture permeability, which are time consuming, and therefore difficult to repeat sufficiently to produce results that apply generally.

BACKGROUND

Resistor networks

Bahr (1997) used random resistor networks to evaluate the bulk electrical conductivity of rocks. In this type of analysis, electrical current is assumed to pass through a network of resistors. Resistors within this network can be defined to be open (i.e., high electrical conductivity) or closed (low conductivity). An electrical potential gradient is applied across the network and used, together with the

resistances in the network, to solve for the current passing through each resistor. The bulk resistivity is then calculated by summing the total current through the network and applying Ohm's Law.

We extend the analysis of Bahr (1997) by considering resistors of variable resistance, and by considering fluid flow through the same network. The resistors represent a network of flat plates with varying apertures, corresponding to varying hydraulic conductivity. The open resistors can be compared the open parts of a fracture, filled with an electrically conductive fluid, whilst the closed resistors can be compared to the background host rock and/or parts of the fault that are closed or cemented with electrically and hydraulically resistive cement. Importantly, the conductivity is controlled not only by the number and aperture of open bonds, but also on their position within the network.

Hydraulic and Electric resistance

The resistance of the bonds can be calculated using an effective electrical and hydraulic resistance at each point within the fracture. In porous media, the hydraulic resistance can be described by Darcy's Law, which relates the volumetric fluid flow rate, Q , to the cross sectional area A , the permeability k , the fluid viscosity μ , and the pressure gradient ∇p :

$$Q = \frac{kA}{12\mu} \nabla p \quad (1)$$

Combining Darcy's Law with the steady-state solution to the Navier-Stokes equations for laminar fluid flow, Brown (1987) deduced an expression Q as a function of the fault aperture b , where l_y is the cross-sectional area of the sample:

$$Q = l_y \frac{b^3}{12\mu} \nabla p \quad (2)$$

These imply the permeability of the fracture is equal to $b^2/12$ (Brown 1989). The hydraulic resistance is given by:

$$R_H = \frac{12\mu\Delta x}{l_y b^3} \quad (3) \quad (\text{Brown 1989; Kirkby et al. 2016}).$$

In a fracture with a variable aperture, this equation can be evaluated pointwise on a discretised grid. This is known as the local cubic law (Brown, 1987).

Likewise, Ohm's Law relates electrical current I to the area A , resistivity ρ , and electrical potential gradient ∇v :

$$I = \frac{A}{\rho} \nabla v = l_y \frac{b}{\rho} \nabla v \quad (4)$$

From these, the electric resistance R_E is given by:

$$R_H = \frac{\rho}{l_y b} \quad (5) \quad (\text{Brown 1989; Kirkby et al. 2016}).$$

Brown (1989) used the above equations to model the electrical current and fluid flow through a single fracture, comparing the results to a global parallel plate model, where the fracture is assumed to consist of a pair of parallel plates with aperture b . Brown (1989) showed that it is necessary to consider variations in aperture within a fracture when the standard deviation of the surface height is greater than 20 % of the mean fracture aperture.

One limitation of the parallel plate model is that assumes that the faces of each fault segment are parallel and horizontal, and that each segment of the fault face is long compared to the aperture. In reality, fracture topography varies strongly within a fracture, with the aperture fluctuations comparable to horizontal distance, and the two faces are not parallel (e.g., Brown and Scholz 1985; Brown 1995). To account for this, a modified parallel plate model can be applied, which uses the solution to the Navier-Stokes equations in a wedge and also corrects for any additional distance in flow path length arising from sloping plates (Brush and Thomson 2003). This model has been shown to provide a good approximation to the full Navier-Stokes equations at low flow velocities such as those likely to be encountered in the subsurface (Brush and Thomson 2003).

Fracture surface topography

The aperture distribution is an important control on the electrical current and fluid flow through a fracture, and controls electrical current and fluid differently (Equations 3 and 5). Therefore it is important to accurately represent fracture aperture distribution to explore the relationship between the two properties. We determined the aperture by first constructing two synthetic opposing fracture surfaces and then separating them by a fixed amount.

The topography of fracture surfaces have been shown to have power spectral density functions of the form:

$$G(f) \propto f^{-\alpha} \quad (6) \quad (\text{Figure 1; Brown 1987})$$

Where G is the power spectral density, f is the spatial frequency, and α is related to the fractal dimension D through

$$\alpha = \frac{7-D}{2} \quad (7)$$

Fractal dimension ranges from about 2.2 to 2.6 in rock fractures (e.g. Brown, 1995; Glover et al., 1998; Matsuki et al., 2006; Ishibashi et al., 2015). Brown (1995) used this relationship to develop an algorithm for generating self-similar fracture surfaces, which uses the inverse Fourier transform to generate fractures with power spectral density functions described by Equations 6 and 7 (Brown, 1995).

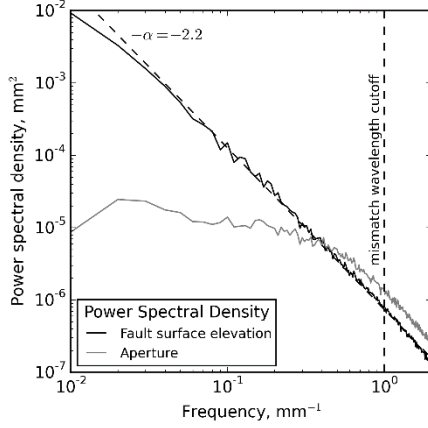


Figure 1. Power spectrum for a synthetic fracture generated in this study. The power spectral density shown for one fault surface (black) and the fault aperture (grey). Also indicated is the mismatch wavelength cutoff used here, and the slope of the power spectrum, α , which is related to the fractal dimension through Equation 7. After Kirkby et al. (2016).

METHOD

Fault surface creation

Two correlated fracture surfaces were generated using the method of Brown (1995) and Matsuki et al. (2006). In this method, the Fourier component a of each fracture surface is related to the fractal dimension D and the spatial frequencies p and q in the x and y direction, where l is the size of the fracture through:

$$\alpha_{1p,q} \propto (p^2 + q^2)^{\frac{4-D}{2}} e^{i2\pi R_1} \quad (8)$$

$$\alpha_{2p,q} \propto (p^2 + q^2)^{\frac{4-D}{2}} e^{i2\pi(R_1 + \gamma R_2)} \quad (9)$$

The surfaces differ by the random component R_2 , which is scaled by γ , which is defined with respect to a mismatch cutoff frequency, f_c . The mismatch cutoff frequency value, and the function relating γ to frequency, has been treated differently by different authors (e.g. Glover et al. 1998a,b; Ogilvie et al. 2006; Matsuki et al., 2006), as discussed by Kirkby et al. (2016). We set γ to 1 above f_c , and a linear function of frequency below f_c (Kirkby et al. 2016):

$$\gamma = \begin{cases} 1 & f > f_c \\ \frac{f}{f_c} & f \leq f_c \end{cases}$$

Once the two fracture surfaces had been generated, they were then scaled and separated by a series of different fixed values for modelling. Overlapping parts of the fractures resulting in negative apertures were set to zero. The resulting apertures were then corrected to effective hydraulic and electric apertures based on the local slope of the two fracture planes and the angle between the two plates (Brush and Thomson 2003; Kirkby et al. 2016). These aperture values were then used to determine the hydraulic and electric resistance (Equations 3 and 5). An example of the resulting fracture surfaces and aperture distribution is shown in Figure 2.

Resistance value

The hydraulic and electrical resistance at each point in the resistor network, $R_{i,j}$, was calculated as a weighted harmonic mean of the resistance of the fracture itself, $R_{f,i,j}$, and that of the surrounding matrix R_m :

$$\frac{\Delta z}{R_{i,j}} = \frac{b}{R_f} + \frac{\Delta z - b}{R_m} \quad (10)$$

Where Δz is a fixed value representing the width of the fracture, and $R_{f,i,j}$ is defined by Equations 3 and 5 using the effective hydraulic and electric aperture described above (Kirkby et al. 2016). Taking a harmonic mean over a fixed width is necessary as it allows zero apertures to be handled without causing infinite resistance. We have set Δz to be equal to the maximum fault aperture, b_{max} , down to a minimum of 0.1 mm, for each fracture (Kirkby et al. 2016). This ensures that the minimum resistivity in any given fracture is equal

to the fluid resistivity, and the maximum is the matrix resistivity. Likewise, the permeability in the fracture ranges from the matrix permeability to $b_{max}^2/12$. If Δz were to be set to some value greater than b_{max} , this would reduce the resistivity and permeability of parts of the fracture with large apertures but have no effect on zero apertures. On the other hand, if Δz is less than b_{max} , this would increase the resistivity above the matrix value, and reduce the permeability below the matrix value, at small apertures. The minimum Δz value was set to avoid very high resistances for fractures with small maximum apertures.

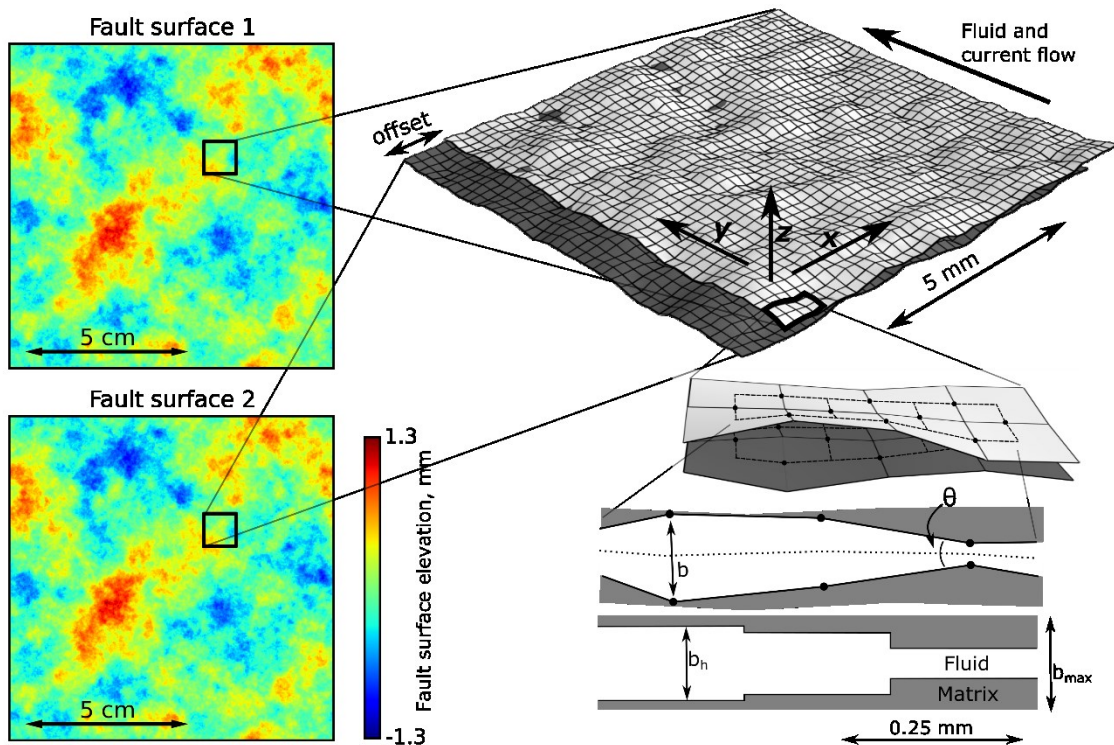


Figure 2. The key features of the setup used for modelling fluid flow and current through fractures including the aperture b and the effective hydraulic aperture b_h , corrected for the angle θ between the two plates and any extra path length resulting from the slope of the two plates. The two surfaces shown have dimensions of 100×100 mm and a horizontal resolution of 0.25 mm. They were created using a fractal dimension of 2.4 and are scaled such that the standard deviation of the surface height equals 0.48 mm. Modified after Kirkby et al. (2016).

Modelling approach

We have followed the approach of Bahr (1997) to solve the resistor network. A potential difference was applied along the fracture, with no current leaving or entering the sides. Kirchhoff's Law was applied in each node, and the electrical potential was assumed to sum to zero in each elementary cell. Likewise, for the permeability, a pressure difference was applied along the fracture, with no-flow boundary conditions set for the fracture sides. Mass was assumed to be conserved in each node and the pressure was assumed to sum to zero in each elementary cell.

A series of equations was then constructed and solved to determine the current and fluid flow in each resistor. The total current and fluid flow through each end of the fracture was then summed and then used in Equations 1 and 4 together with the fixed potential and pressure difference and the Δz value to calculate an effective electrical conductivity and permeability for the fracture.

The resistor network approach implies that the electrical conduction pathways are independent of the absolute resistivities but depend on their ratio. Therefore, we discuss the electrical conductivity of the fracture in terms of the ratio of the rock matrix to fluid resistivity, defined here as m . Likewise, we define the ratio of the matrix to fracture resistivity as M .

Input parameters

Kirkby et al (2016) modelled a total of 760 parameter combinations to identify the main controls on fracture permeability and resistivity. These included incrementally increasing the separation between the fracture surfaces to simulate opening of a fracture, varying the ratio m , and also the rock matrix permeability. A total of 200 repeats on different fractures were carried out, using different random number seeds to generate the fractures. This process was also repeated three different horizontal offsets between the two fracture surfaces.

Here, we present a subset of the modelling results presented by Kirkby et al. (2016), using a fracture with no horizontal offset, a rock matrix permeability of 10^{18} m², and m equal to 10^4 , with modelling carried out over 20 fault separation values. The fractal dimension

was set to 2.4 and the fracture surface heights were scaled such that their standard deviation was equal to 0.48 mm. The fracture resolution was 0.25 mm and the fracture size was 100 × 100 mm; 400 × 400 cells (Kirkby et al. 2016).

RESULTS

Base case

Figure 3a shows the fracture permeability as a function of M . Figure 3b shows fracture permeability and electrical conductivity as a function of arithmetic mean aperture. Figure 4 shows the fluid and current passing through a fracture at two different separation values indicated by white stars and triangles in Figure 3.

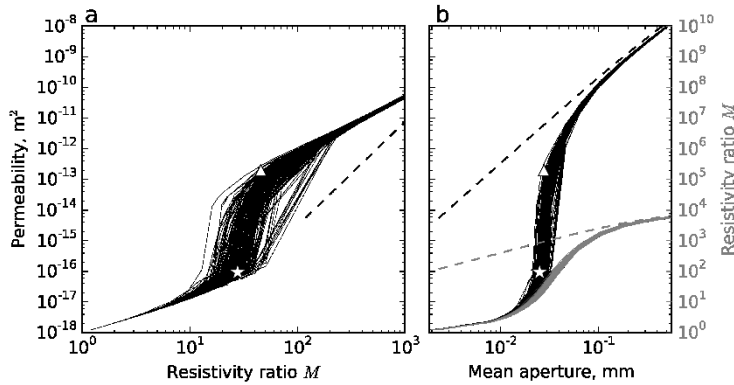


Figure 3. Changes in fracture conductivity (expressed in terms of the ratio M) and permeability as the fracture is opened, for fractures with no offset, within a matrix with permeability 10^{-18} m^2 , with m equal to 10^4 . (a) Permeability as a function of M . (b) Permeability (black) and M (grey) as a function of arithmetic mean fracture aperture. Position of percolation threshold and levelling off point for the fracture in Figure 4 indicated as white stars and triangles respectively. Dashed lines show the permeability and resistivity ratio m for a flat plate model with equivalent mean aperture. After Kirkby et al. (2016).

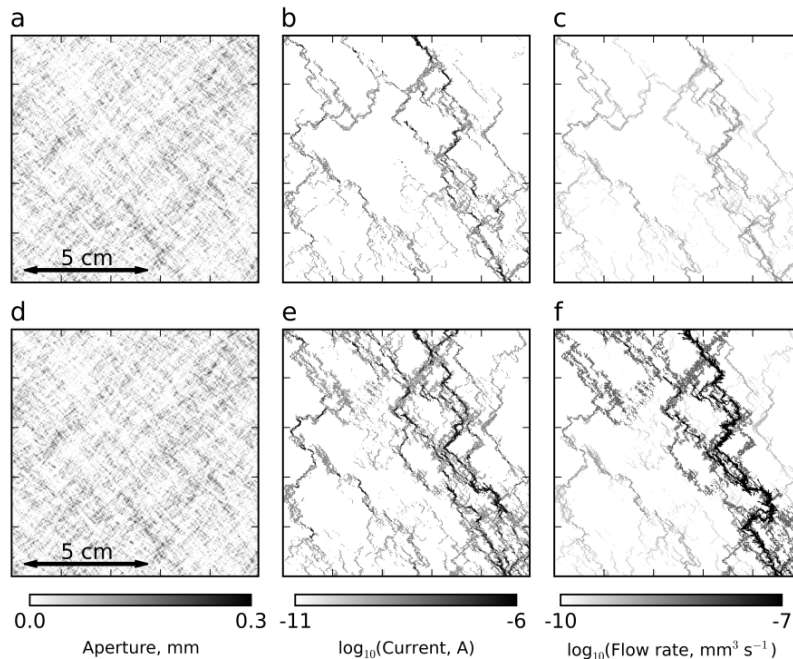


Figure 4. Fluid and current flow along a fracture with no horizontal offset but with two different separation values. (a) Aperture distribution, (b) electrical current and (c) fluid flow for a fracture in which the fault surfaces have been separated by -0.006 mm . This fracture is at its percolation threshold. (d) Aperture distribution, (e) electrical current and (f) fluid flow for a fracture with a separation of 0.000 mm . This fracture is above its percolation threshold. After Kirkby et al. (2016).

The electrical conductivity and permeability increase moderately with aperture at apertures less than about 0.02 mm (Figure 3b; Kirkby et al. 2016). After this point, the fractures reach a percolation threshold and both properties increase more rapidly. Permeability increases by a factor of about 10^4 over an aperture change of about 0.01 mm, while M increases by a factor of 10 over an aperture change of around 0.02 mm. The precise position of the percolation threshold differs for each of the 200 fractures shown in Figure 3, a result of small differences in the fracture topography and resulting aperture distribution arising from the different set of random number seeds used to generate each fracture. Above a mean aperture of 0.03 mm, permeability levels off with respect to aperture, while M levels off later, at a mean aperture of about 0.07 mm.

The rate of increase in electrical conductivity at the percolation threshold is lower than the permeability, and therefore the percolation threshold in permeability can be defined with respect to M . The percolation threshold for the fracture presented in Figure 4 occurs where M is equal to about 30. So when this fracture is below the percolation threshold it increases the permeability by a small amount (to around 10^{-16} m^2), and the resistivity by a factor of 30. A slight increase in aperture ($\sim 0.01 \text{ mm}$) increases the conductivity to a factor of 50, but the permeability increases to $2 \times 10^{-13} \text{ m}^2$.

The fracture shown in Figure 4a-c has a separation of -0.006 mm (i.e. the surfaces were shifted together) and is at the percolation threshold. Figure 4d-f shows the same fracture with a separation of 0 mm ; here it is above the percolation threshold. The percentage contact area between the fracture surfaces in each case is 53 and 49 % respectively. These examples demonstrate the strong differences in the passage of electrical current and fluids through a fracture over its percolation threshold.

Influence of rock and fluid properties, offset and spacing

Kirkby et al. (2016) also modelled eight other m ratios ranging from 3 to 3×10^4 , matrix permeability values of 10^{14} and 10^{16} m^2 , and fault offsets of 0.5, 2.5, and 10.0 mm. In addition, the effect of the mean spacing between faults was assessed by recalculating the effective resistivity and permeability values obtained for individual faults for faulted rock volumes with widths (perpendicular to the fault plane) of 1 mm, 10 mm, and 100 mm.

Varying the matrix permeability does not substantially change the percolation behaviour that is observed, except for raising the permeability at low apertures.

Varying m affects the shape of the resistivity percolation curve and therefore the permeability – resistivity relationship (Kirkby et al. 2016). As might be expected, increasing m increases the value of M at the percolation threshold, M_{PT} . However, M_{PT} decreases as a proportion of m . Where m equals 100, M_{PT} is equal to around 4, i.e. 4% of m . Where m equals 3×10^4 however, $M_{PT} \approx 60$, only 0.2% of m (Kirkby et al. 2016). This is because the matrix contribution to the passage of current through the fracture decreases as m increases, and the aperture distribution controls the fracture resistivity to a greater extent. As a result, the resistivity increase starts later but is sharper than for low values of m (Kirkby et al. 2016).

Increasing the offset between the fault surfaces increases the mean aperture at the percolation threshold to much the same value for both permeability and resistivity (Kirkby et al. 2016). Therefore, the effect on the resistivity – permeability relationship is smaller. The value of M_{PT} at the percolation threshold increases for small offsets ($\leq 0.5 \text{ mm}$) but then decreases again for greater offsets.

Resistivity is affected more by increasing the spacing between faults than permeability. This is because the permeability of an individual fracture typically increases by several orders of magnitude over the percolation threshold, while the conductivity generally increases by a factor of ten or less over the same aperture change (Kirkby et al. 2016). Therefore, even though both properties are reduced proportionally by the same amount when averaged over a wide volume, the effect on electrical conductivity is greater. The effect is lessened in faults with a greater amount of offset: as mentioned above, faults with greater offsets are wider, and therefore take up a greater volume.

CONCLUSION

We have presented modelling that explores the changes in the resistivity and permeability of fractures as they open. As the fault separation increases, both the electrical and hydraulic conductivity increase, initially at a similar rate. Once the fault reaches its percolation threshold, both properties increase more rapidly (Kirkby et al. 2016). The permeability increases by at least three orders of magnitude over changes in aperture of less than 0.1 mm ($< 0.01 \text{ mm}$ for faults with offsets of 0.5 mm or less), while the resistivity only changes by up to one order of magnitude, depending on the ratio of matrix to fluid resistivity.

Permeability increases more rapidly and by a greater amount than resistivity, and therefore the percolation threshold in permeability can also be defined with respect to the resistivity (Kirkby et al. 2016). The ratio of the fracture resistivity to that of the matrix at the percolation threshold, M_{PT} , increases with m , but decreases as a proportion of m . This reflects a decrease in the contribution of the matrix to the overall fracture conductivity as m increases. Increasing the offset on faults increases the mean aperture at the percolation threshold, but it affects both the permeability and resistivity similarly, so the relationship between permeability and resistivity is not strongly affected. Increasing the spacing, however, affects the resistivity much more than the permeability, and so M_{PT} decreases strongly with increasing fault spacing.

The change in mean fault aperture across the percolation threshold varies by less than 0.1 mm . However, the electrical and hydraulic properties can vary strongly. Therefore, small differences in, for example, the local stress field in different areas may be enough to put fractures above their percolation threshold, resulting in large changes in resistivity and permeability (Kirkby et al. 2016). As a result, areas that are similar geologically may exhibit strong differences in electrical and hydraulic properties arising not from lithological differences but from differences in the stress field. These differences may be detectable using techniques such as MT that are sensitive to variations in resistivity with orientation.

ACKNOWLEDGMENTS

We would like to thank Geoscience Australia for a scholarship for this work, and the University of Adelaide for funding support. This work was undertaken with the assistance of resources from the National Computational Infrastructure (NCI), which is supported by the Australian Government. The figures in this extended abstract were generated using the Matplotlib plotting libraries.

REFERENCES

- Archie, G., 1942. The electrical resistivity log as an aid in determining some reservoir characteristics, *Petroleum Transactions of the Australian Institute of Mining, Metallurgical, and Petroleum Engineers*, 146, 54–62.
- Bahr, K., 1997. Electrical anisotropy and conductivity distribution functions of fractal random networks and of the crust: the scale effect of connectivity, *Geophysical Journal International*, 130 (3), 649–660.
- Brown, S.R., 1987. Fluid flow through rock joints: the effect of surface roughness. *Journal of Geophysical Research: Solid Earth*, 92 (B2), 1337-1347.
- Brown, S.R., 1989. Transport of fluid and electric current through a single fracture. *Journal of Geophysical Research: Solid Earth*, 94 (B7), 9429-9438.
- Brown, S.R., 1995. Simple mathematical model of a rough fracture. *Journal of Geophysical Research: Solid Earth*, 100 (B4), 5941-5952.
- Brown, S.R. and Scholz, C.H., 1985. Broad bandwidth study of the topography of natural rock surfaces. *Journal of Geophysical Research: Solid Earth*, 90 (B14), 12575-82.
- Brush, D.J. and Thomson, N.R., 2003. Fluid flow in synthetic rough-walled fractures: Navier-Stokes, Stokes, and local cubic law simulations. *Water Resources Research*, 39 (4), 1-15.
- Caine, J.S., Evans, J.P. and Forster, C.B., 1996. Fault zone architecture and permeability structure. *Geology*, 24 (11), 1025-1028.
- Glover, P.W.J., Matsuki, K., Hikima, R. and Hayashi, K., 1998a. Synthetic rough fractures in rocks. *Journal of Geophysical Research: Solid Earth*, 103 (B5), 9609-9620.
- Glover, P., K. Matsuki, R. Hikima, and K. Hayashi, 1998b. Fluid flow in synthetic rough fractures and application to the Hachimantai geothermal hot dry rock test site, *Journal of Geophysical Research: Solid Earth*, 103 (B5), 9621-9635.
- Kirkby, A., Heinson, G., Holford, S. and Thiel, S., 2015. Mapping fractures using 1D anisotropic modelling of magnetotelluric data: a case study from the Otway Basin, Victoria, Australia. *Geophysical Journal International*, 201(3), pp.1961-1976.
- Kirkby, A., Heinson, G., and Krieger, L., 2016. Relating permeability and electrical resistivity in fractures using random resistor network models. *Journal of Geophysical Research: Solid Earth*, accepted manuscript in press.
- MacFarlane, J., Thiel, S., Pek, J., Peacock, J. and Heinson, G. (2014), Characterisation of induced fracture networks within an enhanced geothermal system using anisotropic electromagnetic modelling, *Journal of Volcanology and Geothermal Research*, 288, 1-7.
- Matsuki, K., Chida, Y., Sakaguchi, K. and Glover, P.W.J., 2006. Size effect on aperture and permeability of a fracture as estimated in large synthetic fractures. *International Journal of Rock Mechanics and Mining Sciences*, 43 (5), 726-755
- Ogilvie, S. R., Isakov, E., and Glover, P. W., 2006. Fluid flow through rough fractures in rocks. II: A new matching model for rough rock fractures, *Earth and Planetary Science Letters*, 241 (3), 454-465.
- Peacock, J. R., Thiel, S., Reid, P., & Heinson, G., 2012. Magnetotelluric monitoring of a fluid injection: Example from an enhanced geothermal system, *Geophysical Research Letters*, 39(18), 1–5.
- Peacock, J. R., Thiel, S., Heinson, G., & Reid, P., 2013. Time-lapse magnetotelluric monitoring of an enhanced geothermal system, *Geophysics*, 78(3), B121–B130.